

Dopant and Current Rate Dependence on the Structural Evolution of P2- $\text{Na}_{2/3}\text{Mn}_{0.8}\text{Zn}_{0.1}\text{M}_{0.1}\text{O}_2$ ($M = \text{Cu}, \text{Ti}$): An Operando Study

Jennifer H. Stansby,^[a, b] Neeraj Sharma,^{*[a]} Maxim Avdeev,^[b] Helen E. A. Brand,^[c] Elena Gonzalo,^[d] Nicholas E. Drewett,^[d] Nagore Ortiz-Vitoriano,^[d, e] and Teófilo Rojo^[f]

Variable current rate operando XRD experiments were performed on the P2- $\text{Na}_{2/3}\text{Mn}_{0.8}\text{Zn}_{0.1}\text{Cu}_{0.1}\text{O}_2$ composition, which displays promising electrochemical properties. The data reveals the reversible formation of a new and previously undetected ordering reflection upon extraction of Na-ions, and that small compositional alterations may dramatically impact structural evolution and electrochemical properties. For P2- $\text{Na}_{2/3}\text{Mn}_{0.8}\text{Zn}_{0.1}\text{Cu}_{0.1}\text{O}_2$ at all current rates examined (25, 50 and 100 mA.g^{-1}), comparable structural evolution on charge is

observed, but the structural evolution on discharge is shown to be significantly influenced by the current applied during the preceding charge step. For both P2- $\text{Na}_{2/3}\text{Mn}_{0.8}\text{Zn}_{0.1}\text{Cu}_{0.1}\text{O}_2$ and P2- $\text{Na}_{2/3}\text{Mn}_{0.8}\text{Zn}_{0.1}\text{Ti}_{0.1}\text{O}_2$ comparable structural evolution is observed only at a slower current rate of 25 mA.g^{-1} . Overall, the structural evolution of these layered materials is shown to be dependent on the cycling history, highlighting the significance of applied current rate during cycling, especially during the initial cycle.

1. Introduction

Due to the wide availability of sodium resources and prospective application in large-scale energy storage systems, sodium-ion batteries (NIBs) have received significant attention among

'next-generation' battery researchers.^[1] Layered oxides (Na_xMO_2 , $M = \text{Ti}, \text{V}, \text{Cr}, \text{Mn}, \text{Fe}, \text{Co}, \text{Ni}, \text{Cu}, \text{Zn}, \text{Li}$, and a mixture of multiples of these elements) are currently dominating the field of NIB cathode materials research owing to their high specific capacities, large compositional diversity and in many cases facile synthesis.^[2] Considering the low cost and low toxicity of starting materials (which are of primary concern for the development of large-scale batteries), Mn-rich layered oxides ($M \geq 0.67 \text{ Mn}$) are an important family of NIB materials.^[3]

The structure of sodium layered oxides can be described as repeating units of MO_6 octahedra, with sodium-ions residing between the metal oxide layers. They are classified based on the system devised by Delmas *et al.* according to the coordination of the sodium-ions (P: trigonal prismatic, O: octahedral), followed by the number of metal oxide layers within the unit cell (typically 2 or 3). A prime symbol (') indicates a distorted phase.^[4] The most common structures are P2 and O3 which differ in their oxygen stacking sequence, ... ABBA ... and ... ABCABC ... respectively.

Studies into the structure-function relationships of these oxides have significantly helped to facilitate the continual development of improved NIB cathode materials. For example, the parent P2- Na_xMnO_2 material displays multiple phase transformations upon cycling and poor cyclability which has been associated with Jahn-Teller distortion of six-coordinate Mn^{3+} ($t_{2g}^3-e_g^1$).^[5] Through tuning the composition with electrochemically active and/or inactive cations, improvements in the structural stability and therefore electrochemical performance have been achieved.^[6] Notable examples (synthesised from non-toxic, earth abundant precursors) include P2- $\text{Na}_{2/3}\text{Mn}_{0.8}\text{Mg}_{0.2}\text{O}_2$, P2- $\text{Na}_{2/3}\text{Mn}_{0.8}\text{Fe}_{0.1}\text{Ti}_{0.1}\text{O}_2$ and P2- $\text{Na}_{2/3}\text{Mn}_{0.8}\text{Zn}_{0.1}\text{Cu}_{0.1}\text{O}_2$.^[6-7]

To acquire accurate information regarding the atomic scale structural evolution of these layered oxides during device

[a] J. H. Stansby, Dr. N. Sharma
School of Chemistry,
University of New South Wales
2052 Sydney, New South Wales (Australia)
E-mail: neeraj.sharma@unsw.edu.au

[b] J. H. Stansby, Prof. M. Avdeev
Australian Centre for Neutron Scattering,
Australia Nuclear Science and Technology Organisation
Kirrawee, 2253 Sydney, New South Wales (Australia)

[c] Dr. H. E. A. Brand
Australian Synchrotron
800 Blackburn Road, 3168 Clayton, Victoria (Australia)

[d] Dr. E. Gonzalo, Dr. N. E. Drewett, Dr. N. Ortiz-Vitoriano
Centre for Cooperative Research on Alternative Energies (CIC energiGUNE),
Basque Research and Technology Alliance (BRTA)
Parque Tecnológico de Alava
Albert Einstein 48, 01510 Vitoria-Gasteiz (Spain)

[e] Dr. N. Ortiz-Vitoriano
Ikerbasque, Basque Foundation for Science
María Díaz de Haro 3, 48013 Bilbao (Spain)

[f] Prof. T. Rojo
Departamento de Química Inorgánica,
Universidad del País Vasco UPV/EHU
P.O. Box 664, 48080 Bilbao (Spain)

Supporting information for this article is available on the WWW under <https://doi.org/10.1002/cmtd.202000075>

An invited contribution to a joint Special Collection between Batteries & Supercaps and Chemistry—Methods on In Situ and Operando Methods for Energy Storage and Conversion. Please visit chemistry-methods.org/collections to view all contributions.

© 2021 The Authors. Published by Wiley-VCH GmbH. This is an open access article under the terms of the Creative Commons Attribution Non-Commercial License, which permits use, distribution and reproduction in any medium, provided the original work is properly cited and is not used for commercial purposes.

operation, the ability to study cathode materials in situ or operando (i.e. in real time) is crucial because the active materials are not at equilibrium during device operation.^[8] If on the other hand ex situ studies, in which electrode materials are extracted from cells which have been cycled, are performed, the results may be perturbed by contamination while handling the sample between battery cycling and characterisation, or relaxation effects.^[9,10]

The value of in situ studies has been demonstrated through investigating the rate dependent structural evolution of P2- $\text{Na}_{0.67}\text{Mn}_{0.8}\text{Mg}_{0.2}\text{O}_2$.^[9] While ex situ XRD data showed the presence of both *Cmcm* and *P6₃/mmc* phases at the discharged state following a charge cycle at 12 mA.g^{-1} and a discharge cycle at 100 mA.g^{-1} , in situ synchrotron XRD data showed the presence of solely the *P6₃/mmc* phase at the discharged state under the same cycling conditions. Therefore, the work showed that cycling at lower applied discharge currents (100 mA.g^{-1} cf. 200 mA.g^{-1} and 400 mA.g^{-1} rates) produced higher capacities than higher applied current rates as intuitively expected. Note, in this work^[9] the rationale for the capacity differences was proposed to be related to the quantity of *Cmcm* phase formed near the discharged state (as evidenced in the ex situ studies).

Dramatic differences in the structural evolution of P2- $\text{Na}_{2/3}\text{Mn}_{1/3}\text{Fe}_{2/3}\text{O}_2$, probed using time resolved in situ synchrotron XRD were also found.^[10] The high rate performance of the material was attributed to the preservation of the P2- type structure and absence of significant disorder in the layered structure near the charged state. At slower rates, the disordered structure was found to persist during subsequent discharge cycles. Further work in the P2- $\text{Na}_{2/3}\text{M}_y\text{Fe}_{1-y}\text{O}_2$ series, the P2- $\text{Na}_{2/3}\text{Mn}_{0.9}\text{Fe}_{0.1}\text{O}_2$ composition was synthesised and its structural evolution examined at various current rates (7.5 mA.g^{-1} , 15 mA.g^{-1} and 80 mA.g^{-1}).^[11] At the higher rate of 80 mA.g^{-1} , two P2- type phases were observed throughout whereas at lower current rates, the two-phase mixture was found to transform into a single phase at the charged state. The (nonequilibrium) differences in structural evolution detected using synchrotron X-ray powder diffraction were attributed to kinetic limitations upon applying a higher current. Further modification of the P2- $\text{Na}_{2/3}\text{Mn}_{0.9}\text{Fe}_{0.1}\text{O}_2$ system by substitutions for Mn by both electrochemically active (Ni, Co, Cu) and/or electrochemically inactive dopants (Zn, Al, Ti, Li, Mg) have been widely explored.^[6,7b,12] Given the promising electrochemical performance reported for P2- $\text{Na}_{2/3}\text{Mn}_{0.8}\text{Ti}_{0.1}\text{Fe}_{0.1}\text{O}_2$ (second charge/discharge capacity of $146.57/144.16\text{ mAh.g}^{-1}$ and 87.7% capacity retention of the second discharge capacity when cycled between 2.0–4.0 V at C/10), the variable current cycling structural evolution of the material was probed at current rates as high as 526 mA.g^{-1} (4C) over a wide voltage window of 1.5–4.2 V.^[13] The data revealed that the application of high current rates may suppress structural transitions due to kinetic limitations restricting the change in sodium content upon cycling. At lower current rates ($\leq 44\text{ mA.g}^{-1}$), when maximum desodiation takes place, a collapse in the *c* lattice parameter (indicative of transition metal migration) was observed, followed by a P2-OP4 transition at the charged state.^[14] Analysis of the rate of volume and Na occupancy change showed no clear

correlation between the rates of structural parameter change and the applied current.

Overall, the abovementioned studies demonstrate the value of current-dependent structural information in developing an understanding of how electrode materials function during device operation in real time, under real world conditions. In turn this knowledge can be used to optimise the composition and cycling conditions to advance Na-ion battery cathode materials. Herein the variable current rate structural evolution of the promising cathode material, P2- $\text{Na}_{2/3}\text{Mn}_{0.8}\text{Zn}_{0.1}\text{Cu}_{0.1}\text{O}_2$, made from earth abundant resources is examined via operando synchrotron XRD. Comparisons to previously reported Mn-rich layered oxides examined under varying current rates are made and an additional low-rate experiment is performed on the related P2- $\text{Na}_{2/3}\text{Mn}_{0.8}\text{Zn}_{0.1}\text{Ti}_{0.1}\text{O}_2$ composition. The subtle substitution of Cu^{2+} for Ti^{4+} leads to a distinct change in Mn oxidation state of the layered materials (+3.66 vs. +3.41) and influences the interaction between the transition metal ions which in turn effects the materials structural evolution and thus electrochemical properties.^[15] It is therefore of interest to explore and compare the behaviour of these high-performance materials, notably made from earth abundant elements, upon varying the applied current rates to develop a deeper understanding of how the choice of dopant(s) and cycling conditions influence the materials structural evolution.

The results reveal the occurrence of an ordering reflection for the P2- $\text{Na}_{2/3}\text{Mn}_{0.8}\text{Zn}_{0.1}\text{Cu}_{0.1}\text{O}_2$ cathode only, despite the very similar composition for both materials. The superior electrochemical performance of P2- $\text{Na}_{2/3}\text{Mn}_{0.8}\text{Zn}_{0.1}\text{Cu}_{0.1}\text{O}_2$ suggests that reversible ordering at the charged state may assist in stabilising these layered oxides at low sodium contents. Moreover, the history-dependent structural evolution demonstrated for both P2- $\text{Na}_{2/3}\text{Mn}_{0.8}\text{Zn}_{0.1}\text{Cu}_{0.1}\text{O}_2$ and P2- $\text{Na}_{2/3}\text{Mn}_{0.8}\text{Zn}_{0.1}\text{Ti}_{0.1}\text{O}_2$ highlights the value in optimizing the cycling conditions, especially during the initial cycles, for these cathode materials.

2. Results and Discussion

2.1. P2- $\text{Na}_{2/3}\text{Mn}_{0.8}\text{Zn}_{0.1}\text{Cu}_{0.1}\text{O}_2$

2.1.1. Structural Evolution of P2- $\text{Na}_{2/3}\text{Mn}_{0.8}\text{Zn}_{0.1}\text{Cu}_{0.1}\text{O}_2$

Initially, variable current rate operando XRD experiments were performed on the P2- $\text{Na}_{2/3}\text{Mn}_{0.8}\text{Zn}_{0.1}\text{Cu}_{0.1}\text{O}_2$ composition; details regarding cycling conditions can be found in Table S1 in the Supporting Information. The initial refinement for the dataset (Figure 1) suggests that the uncycled material adopts *P6₃/mmc* symmetry with refined lattice parameters of $a = 2.9080(2)\text{ \AA}$ and $c = 11.1867(1)\text{ \AA}$ – crystallographic details can be found in Table S2 in the Supporting Information. As noted in Figure 1, the origin of the peak at $2\theta = 15.15^\circ$ (corresponding to a *d* spacing of 2.48 \AA) is not clear and is therefore assigned as an unknown impurity. Throughout cycling at variable current rates and between different voltage ranges, the phase evolution is primarily solid solution and was therefore modelled with a

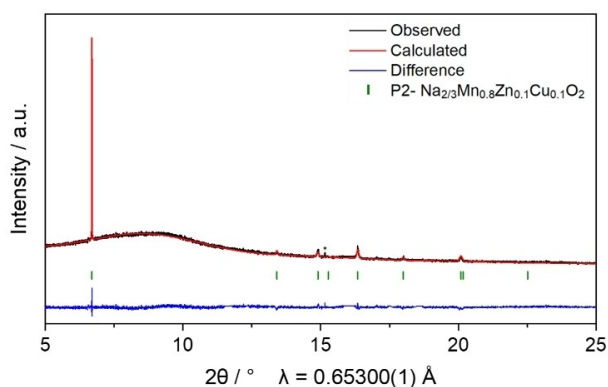


Figure 1. Rietveld refined fit of the uncycled P2- $\text{Na}_{2/3}\text{Mn}_{0.8}\text{Zn}_{0.1}\text{Cu}_{0.1}\text{O}_2$ electrode, within a modified Na half-cell. The asterisk indicates an unknown impurity.

single P2- type phase (space group $P6_3/mmc$), unless specified otherwise.

Shortly after the initial charge at the lowest applied current rate of $25 \text{ mA}\cdot\text{g}^{-1}$ or $C/10$, a second P2- type phase forms, see Figures 2 and S1 in the Supporting Information. As shown in Figure S1 in the Supporting Information, there is significant overlap between the original P2 phase and new P2 phase, which follows an almost identical evolution (increase in the c lattice parameter and decrease in the a lattice parameter during charge). Due to the significant overlap in reflections, the atomic parameters for the second P2 phase were not refined. Around 3.5 V or 155 minutes, only a single P2 phase can be identified and an additional reflection at $2\theta = 14.42^\circ$, which corresponds to a d spacing of 2.6 \AA , appears. The single additional reflection indicates a subtle lattice distortion or some form of ordering, such as Na/vacancy. For Na vacancy ordering, a greater number of new reflections corresponding to a cell superstructure and a more stepped voltage profile might be expected (depending

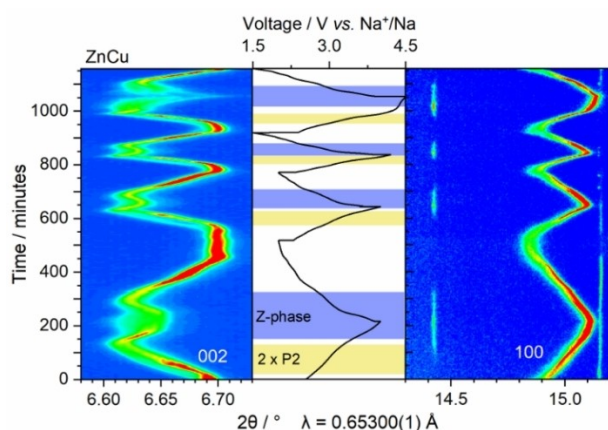


Figure 2. Selected 2θ regions of operando synchrotron XRD data and potential profile as a function of time highlighting the evolution of the 002 and 100 reflections for P2- $\text{Na}_{2/3}\text{Mn}_{0.8}\text{Zn}_{0.1}\text{Cu}_{0.1}\text{O}_2$ as well as the reversible formation of an ordering reflection around 14.4° (2.6 \AA). Yellow regions represent two-phase regions and purple regions represent transformation into possibly the Z phase, see Figure 4 for further details.

on the ordering).^[16] After the appearance of the ordering reflection, a shift in the 002 reflection towards higher 2θ values can be seen in Figure 2, corresponding to a collapse in the c lattice parameter (Figure 3). The shift to higher angles is accompanied by an intensity reduction close to 4.0 V, which indicates the possible onset of an intergrowth structure or transition metal migration into the sodium layer as the sodium content reaches a minimum at the charged state.^[13] Given that the presence of Zn dopants have been evidenced in the sodium layer of P2- $\text{Na}_{0.67}\text{Ni}_{0.23}\text{Mn}_{0.67}\text{Zn}_{0.1}\text{O}_2$ using atomic resolution STEM-HAADF imaging,^[17] it would seem feasible that migration of Zn into the Na layer for the P2- $\text{Na}_{2/3}\text{Mn}_{0.8}\text{Zn}_{0.1}\text{Cu}_{0.1}\text{O}_2$ composition could be taking place.

On discharge to $\sim 2.1 \text{ V}$ (~ 456 minutes), the reverse processes take place – a near linear increase in the a lattice parameter and a brief increase in the c lattice parameter followed by a steady decrease. Below $\sim 2.1 \text{ V}$, both the a and c lattice parameters stabilise. However, no ordering reflection is found at the discharged state.

On the 2nd and 3rd charge/discharge cycles a very similar evolution in terms of lattice parameters and phase transitions occurs. As shown by Figure 4, the same phase evolution ($\text{P2} \rightarrow 2 \times \text{P2} \rightarrow \text{P2} \rightarrow \text{Z}$) is observed on charge throughout the experiment despite varying the cycling conditions. The nature of the phases formed does however vary depending on the current and voltage window applied. For example, comparing Figures 4a and b indicates that application of a lower current rate within the same voltage range results in a more disordered charged state structure (evidenced by a significantly broader and less intense reflection). This, when referring to Table S1 in the Supporting Information, is intuitively expected because at the lower current rate of $25 \text{ mA}\cdot\text{g}^{-1}$, more Na is removed from the structure (higher capacity). Table S1 in the Supporting Information also shows that charging the material to higher voltages causes more Na to be removed from the structure (higher capacity), possibly destabilising the structure. Figure 4e

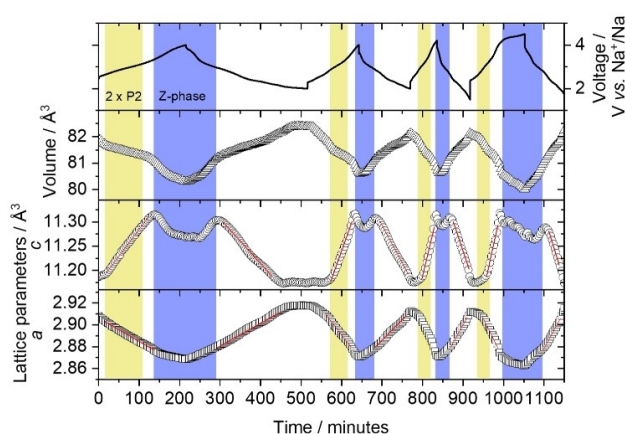


Figure 3. Evolution of the cell voltage, unit cell volume, c lattice parameter and a lattice parameter as a function of time for P2- $\text{Na}_{2/3}\text{Mn}_{0.8}\text{Zn}_{0.1}\text{Cu}_{0.1}\text{O}_2$. Yellow regions represent two phase regions and purple regions represent transformation into possibly the Z phase. The red lines show the linear regions used to analyse the rate of change lattice parameters (see also Figure 8).

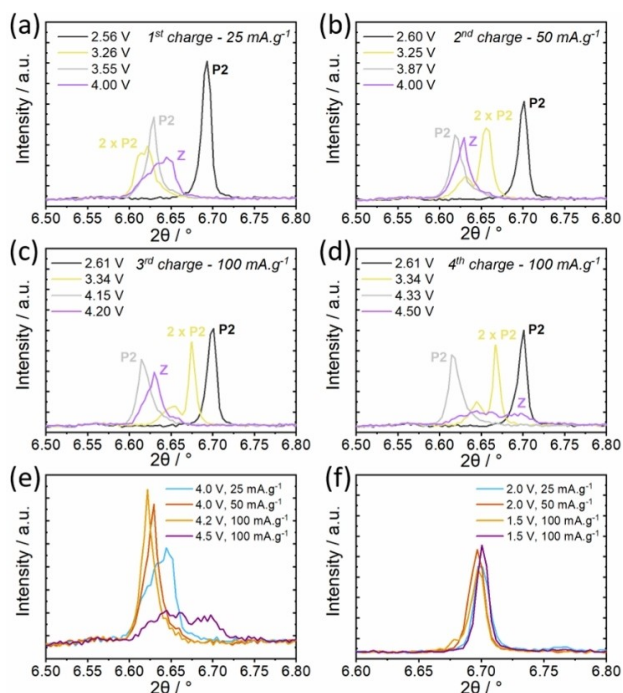


Figure 4. a–d) Selected operando XRD data highlighting the evolution of the P2- $\text{Na}_{2/3}\text{Mn}_{0.8}\text{Zn}_{0.1}\text{Cu}_{0.1}\text{O}_2$ (002) reflection under different cycling conditions and e–f) an overlay of the (002) reflection at each charged/discharged state examined.

experimentally demonstrates this to be the case. At higher voltages a significant drop in peak intensity and dramatic increase in broadness can be observed for the 002 reflection, indicating more disorder and an intergrowth of P2- and O3-type layers at the charged state, which has been termed the Z phase in the literature.^[18] This contrasts to extending the voltage window from 2.0 V to 1.5 V upon discharge which (in addition to increasing the applied current rate) does not appear to significantly alter the structure formed at the discharged state, as shown by Figure 4f.

On the final cycle, however, when charged above 4.3 V, a plateau in the potential profile is observed (see Figure 5), which is associated with the onset of a phase transformation. During the potential plateau region, a significant drop in the intensity of the 002 reflection occurs as shown in Figures 4 and 6, corresponding to the presence of a Z phase with disorder along the *c* axis. Furthermore, the reflection at $2\theta = 14.42^\circ$ (2.6 \AA) is more intense in this region, see Section 2.1.3. for further details. Recovery in intensity of the 002 reflection is not observed until below 2.69 V on discharge where the P2 phase reforms, see Figure 6. No new reflections at larger 2θ values, corresponding to new phases such as OP4 or O2, are observed during this low intensity period (charge to 4.5 V) for the 002 reflection.

In combination with the extremely low theoretical Na content of 0.01, shown in Table S1 in the Supporting Information, calculated from the experimentally determined capacities, the plateau region observed could be indicative of anion redox activity.^[19] The participation of oxygen redox seemingly enables the much larger capacity of 222 mA.g^{-1} to be delivered when

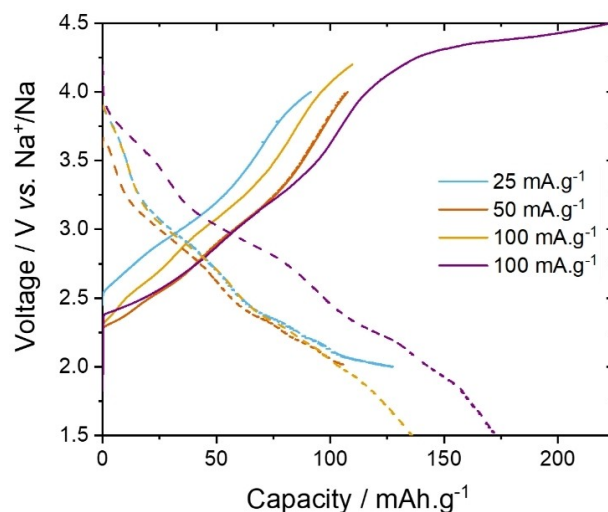


Figure 5. Voltage vs. capacity curves observed during the operando cycling experiment. A distinct plateau region can be seen above 4.3 V.

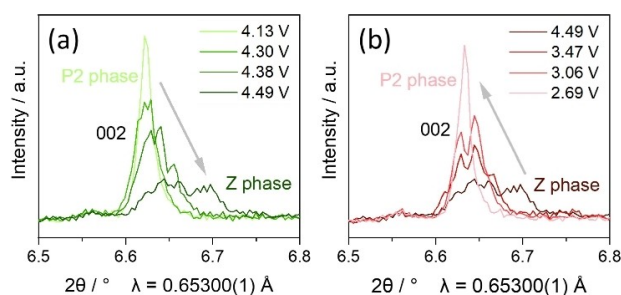


Figure 6. Selected operando XRD data highlighting the evolution of the P2- $\text{Na}_{2/3}\text{Mn}_{0.8}\text{Zn}_{0.1}\text{Cu}_{0.1}\text{O}_2$ (002) reflection close to the 4.5 V charged state upon a) charge and b) discharge showing reversible formation of the Z-phase.

charged to 4.5 V compared with the capacity of 109 mA.g^{-1} delivered on the previous cycle when charged to 4.2 V. Moreover, the high capacity of 173 mA.g^{-1} and reversible structural evolution displayed on the subsequent discharge cycle suggests that any oxygen redox reactions that may be taking place are highly reversible.

Upon charging up to 4.5 V, oxygen redox activity has also been reported for the Mn-rich cathode materials P2- $\text{Na}_{0.78}\text{Ni}_{0.23}\text{Mn}_{0.69}\text{O}_2$, P2- $\text{Na}_{0.78}\text{Li}_{0.25}\text{Mn}_{0.75}\text{O}_2$ and P2- $\text{Na}_{2/3}\text{Mn}_{7/9}\text{Zn}_{2/9}\text{O}_2$.^[19–20] Furthermore, the oxidation of oxygen anions at low sodium concentrations has been associated with increased structural stability owing to reduced coulombic repulsion between the adjacent oxygen layers, provided that no O_2 gas is released in the process.^[21]

2.1.2. Rate Dependence of the Phase Evolution of P2- $\text{Na}_{2/3}\text{Mn}_{0.8}\text{Zn}_{0.1}\text{Cu}_{0.1}\text{O}_2$

Table 1 details the Na concentrations at which the phase transformations begin to take place under the varying cycling conditions examined (the corresponding voltages can be found

Table 1. The Na content (x) in $\text{Na}_x\text{Mn}_{0.8}\text{Zn}_{0.1}\text{Cu}_{0.1}\text{O}_2$ calculated using the values in Table S1 in the Supporting Information and the voltage vs. capacity data shown in Figure 5, at which the additional reflection at $2\theta = 14.42^\circ$ (2.6 \AA) appears, a second P2- type phase forms and onset of the Z phase formation takes place, along with the corresponding cycling conditions applied for each cycle.

Cycle	Current/ [mA.g ⁻¹]	Voltage/ [V]	x in $\text{Na}_x\text{Mn}_{0.8}\text{Zn}_{0.1}\text{Cu}_{0.1}\text{O}_2$	Ordering reflection	Z
1	25	4.0–2.0	0.57	0.4	0.33
2	50	4.0–2.0	0.58	0.36	0.35
3	100	4.2–1.5	0.54	0.36	0.31
4	100	4.5–1.5	0.62	0.39	0.23

in Table S1 in the Supporting Information). It would appear from Table 1 that different structures preferentially form within distinct Na concentrations, irrespective of the cycling conditions: $0.62 \geq x \geq 0.57$ for the $2 \times \text{P2}$ region; $0.40 \geq x \geq 0.36$ for the ordering reflection; and $0.35 \geq x \geq 0.23$ for Z phase formation. However, it is interesting to note that intergrowth of the Z phase on the 4th cycle, upon charging up to the highest voltage of 4.5 V at 100 mA.g^{-1} , does not begin until a significantly lower Na concentration of 0.23 compared to the value 0.31 observed when charged to 4.2 V at the same current rate of 100 mA.g^{-1} , which is reflected by the formation voltages of 4.15 V and 4.32 V respectively. The delayed onset of Z phase formation could be due to the difference in cycling history – when charged to 4.2 V, the previous cycle was at a current of 50 mA.g^{-1} whereas the charge cycle up to 4.5 V was preceded by a cycle at a higher current rate of 100 mA.g^{-1} . Moreover, additional contributions from anion redox activity above 4.3 V may alter the charge compensation mechanism and therefore structural evolution at low Na concentrations.

2.1.3. Nature of the $2\theta = 14.42^\circ$ (2.6 \AA) Reflection

Throughout the experiment, the reflection at $2\theta = 14.42^\circ$ (d -spacing of 2.6 \AA) appears at a similar state of charge and subsequently disappears at a similar state of discharge (in terms of Na concentration), see Table 1. The corresponding voltages are shown in Table S3. The peak position and integrated peak intensity of this reflection is plotted as a function of voltage in Figure 7. Given that the position of the reflection is nearby the 100 reflection ($\sim 15.1^\circ$ or 2.48 \AA), it is likely associated with ordering in the ab plane. Upon charging, Figure 7a appears to show a very slight shift in peak position to smaller values of 2θ , which is most noticeable on the first charge cycle when the lowest current of 25 mA.g^{-1} was applied. However, given the minimal magnitude of the shift ($\sim 0.005^\circ$), this is relatively insignificant, thus supporting the stationary nature of the reflection observed in Figure 2. On discharge, no clear trend in the peak position as a function of voltage can be observed (Figure 7a) demonstrating that the reflection position is stable during Na extraction and reinsertion.

Considering the integrated peak intensities shown in Figure 7b, at the lower applied current rate of 25 mA.g^{-1} , a gradual

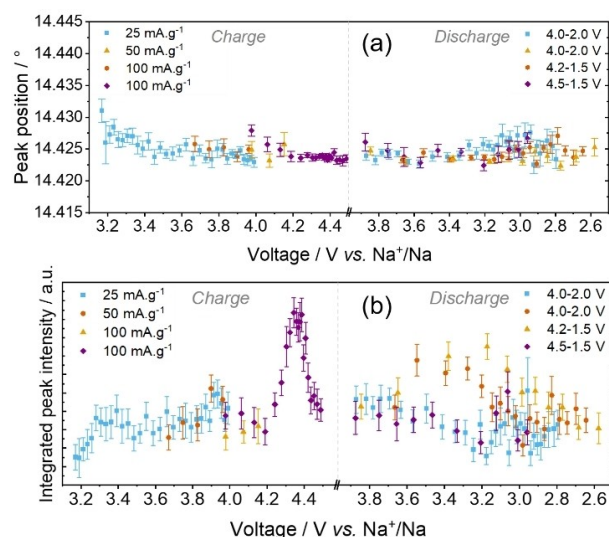


Figure 7. Single peak fit results showing a) the peak position and b) the integrated peak intensity of the ordering reflection at $2\theta = 14.42^\circ$ (2.6 \AA), plotted as a function of voltage for each of the four charge cycles.

increase in intensity is observed and this is followed by a plateau in the peak intensity up to the 4.0 V charged state. Upon discharge, there appears to be a general trend towards lower intensities as the voltage drops. A clear variation as a function of voltage can be seen during the 4th cycle upon charging the cell to 4.5 V at a current rate of 100 mA.g^{-1} . A sharp increase in the peak intensity takes place between 4.2–4.38 V, which is followed by a drop back to the intensity initially observed upon the appearance of the reflection. While the origin of this change in intensity is unknown, it could be associated a momentary change in structure within the ab plane.

The observed reflection position of $d = 2.6 \text{ \AA}$ is unusual with respect to the literature and is suspected to be related to the ab plane. Transition metal ordering has been widely observed for Mn and Ni containing layered oxides at a d -spacing of approximately $3.8\text{--}4.5 \text{ \AA}$.^[18,22] However, unlike the reversible ordering phenomenon at the charged state observed for P2- $\text{Na}_{2/3}\text{Mn}_{0.8}\text{Zn}_{0.1}\text{Cu}_{0.1}\text{O}_2$, the honeycomb type ordering between Mn and Ni has been reported for uncycled electrode materials. Moreover, neutron scattering techniques were typically used to detect this honeycomb type ordering due to the greater difference in neutron scattering lengths vs. X-ray scattering factors for these elements.^[18] Using high energy synchrotron X-ray diffraction, additional ordering reflections associated with Na-ion and vacancy ordering have been reported for Mn and Ni containing compositions. The existence of Na/vacancy superstructure ordering in the P2- $\text{Na}_x\text{Mn}_{2/3}\text{Ni}_{1/3}\text{O}_2$ composition was detected by Lee *et al.* in the pristine (uncycled) and discharged (2.5 V) XRD patterns.^[22a] Small peaks were detected at d -spacings of 3.27 \AA , 3.14 \AA and 3.04 \AA . Several Na-ion ordering motifs including honeycomb, diamond, row and large zigzag (LZZ), were computationally modelled for the pristine $\text{Na}_{2/3}\text{Mn}_{2/3}\text{Ni}_{1/3}\text{O}_2$ composition and the LZZ model was found to be at least 20 meV f.u.^{-1} lower in energy relative to the other models.

Furthermore, the superstructure peaks in the XRD patterns were found to be consistent with the average distance between nearest neighbour Na-ions in the proposed LZZ pattern. The absence of ordering reflections for the uncycled P2- $\text{Na}_{2/3}\text{Mn}_{0.8}\text{Zn}_{0.1}\text{Cu}_{0.1}\text{O}_2$ electrode and significantly different d spacing at the charged state, suggests that there is no LZZ ordering of the Na-ions.

In a comparative study, Gutierrez et al. detected LZZ ordering in P2- $\text{Na}_{0.67}\text{Mn}_{0.67}\text{Ni}_{0.33}\text{O}_2$ but not P2- $\text{Na}_{0.67}\text{Mn}_{0.75}\text{Ni}_{0.25}\text{O}_2$.^[22b] It was therefore proposed that increasing the concentration of higher energy Mn–Na–Mn sites disrupts the LZZ Na/vacancy ordering, which is likely the case for P2- $\text{Na}_{2/3}\text{Mn}_{0.8}\text{Zn}_{0.1}\text{Cu}_{0.1}\text{O}_2$ as well. Upon charging, the ordering was found to change from LZZ to rows initially with one row of Na(1) and two Na(2) rows alternating in the plane at $x=0.5$ and subsequently alternating rows of solely Na(1) or Na(2) in a single layer. However, due to stacking faults caused by the P2 to O2 phase transformation, Lee et al. were not able to detect superstructure peaks at the charged state. Following reinsertion of Na-ions during discharge the ordering reflections reformed, suggesting that the Na/vacancy ordering is preferred at a Na concentration of approximately $x=2/3$. As shown in Table 1, the P2- $\text{Na}_x\text{Mn}_{0.8}\text{Zn}_{0.1}\text{Cu}_{0.1}\text{O}_2$ ordering reflection also appears to preferentially form around a particular Na concentration, $x\approx 0.38$, irrespective of the cycling conditions. Moreover, no P2 to O2 phase transition takes place so perhaps the ordering reflection could correspond to the Na ordering in rows. However, if this were the case, the ordered reflection would be expected to appear around 2.87 \AA , i.e., correspond to the distance between nearest neighbour Na-ions, as oppose to 2.6 \AA .

2.1.4. Variable Current Lattice Parameter Response Rates in P2- $\text{Na}_{2/3}\text{Mn}_{0.8}\text{Zn}_{0.1}\text{Cu}_{0.1}\text{O}_2$

Figure 8 shows the response (rate of change) of the a and c lattice parameters to the various cycling conditions examined. Considering the third and fourth cycles, minute differences can be observed indicating that, in contrast to the phase evolution, extending the voltage window has little impact on the lattice parameter response rates. However, for both the a and c lattice parameters, increasing the current rate appears to result in a greater rate of change. Additionally, for all cycles the response upon charging seems to be equal to or exceed the response upon discharge, suggesting that the mobility of Na-ions upon extraction is greater than upon reinsertion. Interestingly, the response of cell volume to applied current for the previously reported P2- $\text{Na}_{2/3}\text{Mn}_{0.8}\text{Fe}_{0.1}\text{Ti}_{0.1}\text{O}_2$ did not show a clear correlation with the applied current.^[13]

2.1.5. Current-Structure-Function Relationships in P2- $\text{Na}_{2/3}\text{Mn}_{0.8}\text{Zn}_{0.1}\text{Cu}_{0.1}\text{O}_2$

Electrochemically, a lower discharge capacity was observed for the operando half-cell on the 2nd cycle for which the applied current was doubled relative to the 1st cycle, while keeping the

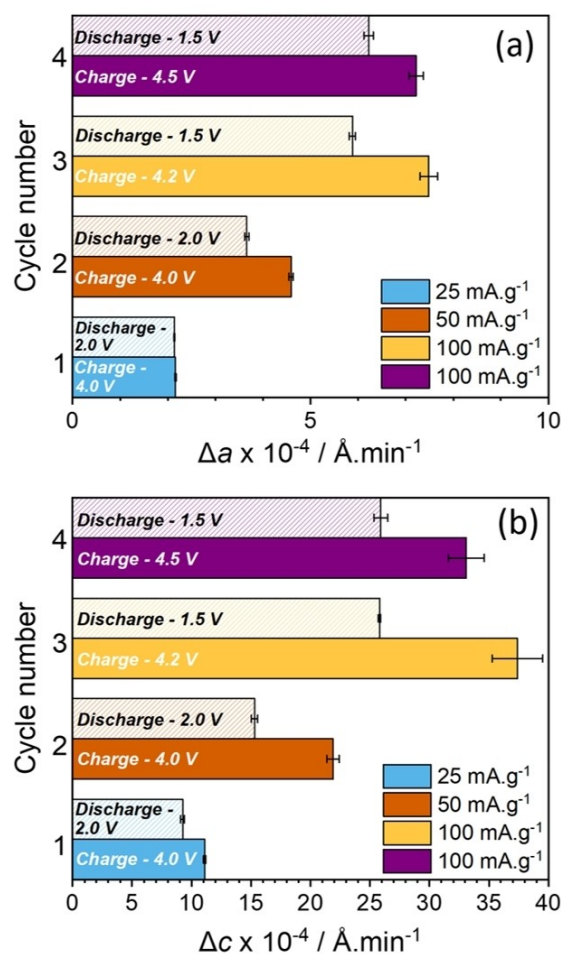


Figure 8. Rates of change of a) the a and b) the c lattice parameters during cycling as a function of applied current rate derived from the linear fits shown in Figure 3.

voltage window constant. The lower capacity upon increasing the current may be attributed to kinetic limitations which restrict the amount of sodium ions that can diffuse into the material, as reported for the P2- $\text{Na}_{2/3}\text{Mn}_{0.8}\text{Fe}_{0.1}\text{Ti}_{0.1}\text{O}_2$ system.^[13] Interestingly, for P2- $\text{Na}_{2/3}\text{Mn}_{0.8}\text{Fe}_{0.1}\text{Ti}_{0.1}\text{O}_2$, increasing the applied current density to $44 \text{ mA} \cdot \text{g}^{-1}$ or higher was found to also suppress structural transitions. For the P2- $\text{Na}_{2/3}\text{Mn}_{0.8}\text{Zn}_{0.1}\text{Cu}_{0.1}\text{O}_2$ cathode, the same (reversible) phases transformations are observed at the highest current rate of $100 \text{ mA} \cdot \text{g}^{-1}$ but the onset of Z phase formation does appear to take place at higher voltages upon increasing the applied current – approximately 3.3 V at $25 \text{ mA} \cdot \text{g}^{-1}$, 3.9 V at $50 \text{ mA} \cdot \text{g}^{-1}$ and 4.2 V at $100 \text{ mA} \cdot \text{g}^{-1}$ (noting that there may be marginal delays between the real-time electrochemistry and XRD data collection particularly close to the charged state, when the rate of change in the voltage is typically greatest) – which is likely due to the higher voltage required to achieve the same level of desodiation upon applying a higher current.

Comparing the 3rd and 4th charge cycles for which the same current of $100 \text{ mA} \cdot \text{g}^{-1}$ was applied but the voltage range was increased from $2.0\text{--}4.2 \text{ V}$ to $1.5\text{--}4.5 \text{ V}$, the P2- $\text{Na}_{2/3}\text{Mn}_{0.8}\text{Zn}_{0.1}\text{Cu}$

$_{0.1}\text{O}_2$ material delivers approximately double the capacity (109 mAh.g^{-1} vs. 222 mAh.g^{-1}). Notably, reversible structural evolution (i.e., recovery of a single P2 phase on the subsequent discharge) is observed during both the 3rd and 4th cycles, indicating the feasibility of exploiting a wider voltage range to access additional capacity, without compromising the materials structural stability. At the higher voltage, it is possible that additional short-range structural changes which cannot be detected using X-ray diffraction (which probes long-range order) are taking place. For example, anion redox activity which has been reported in related layered oxide materials such as $\text{P2-Na}_{2/3}\text{Mn}_{7/9}\text{Zn}_{2/9}\text{O}_2$ may contribute towards the enhanced capacity.^[20a]

When cycled between 4.0–2.0 V and upon applying a current rate of 40 mAh.g^{-1} from the onset, the structural evolution $\text{P2-Na}_{2/3}\text{Mn}_{0.8}\text{Zn}_{0.1}\text{Cu}_{0.1}\text{O}_2$ presents as a single phase solid-solution reaction, see details in ref.^[15] Stable lattice parameters upon discharge are observed with application of the higher initial current rate (40 mA.g^{-1}), which is consistent with the findings from the initial operando XRD experiments shown in Figure 2. It is interesting to note that application of a lower initial current rate of 25 mA.g^{-1} or C/10 (Figure 3) compared to 40 mA.g^{-1} or C/6 (Figure S2 in the Supporting Information) results in dramatically different structural transitions upon charging. At the lower current rate of 25 mA.g^{-1} , presence of an additional P2 phase, appearance of an ordering reflection, and 002 reflection intensity loss (indicating formation of the Z phase) above 3.3 V are observed. In contrast, at the high current rate of 40 mA.g^{-1} , the evolution is predominantly single phase, no ordering reflections are detected and the transition to Z phase is not observed during the 1st cycle. The evolution on discharge at a lower current rate of 25 mA.g^{-1} (C/10) is however comparable to the 40 mA.g^{-1} rate, predominantly single phase and particularly stable near the 2.0 V discharged state. Overall, the comparison between the two relatively slow current rates on the first cycle highlights the structural sensitivity, especially of the sodium deficient composition (i.e., at high voltages), to applied current rate.

Following the initial 25 mA.g^{-1} cycle and increasing to higher rates ($> 40 \text{ mA.g}^{-1}$), $\text{P2-Na}_{2/3}\text{Mn}_{0.8}\text{Zn}_{0.1}\text{Cu}_{0.1}\text{O}_2$ retains similar evolution to that observed on the initial cycle at 25 mA.g^{-1} (Figure 3) rather than the simple single phase evolution observed when initially cycled at 40 mA.g^{-1} (Figure S2 in the Supporting Information) which indicates that the phase evolution of $\text{P2-Na}_{2/3}\text{Mn}_{0.8}\text{Zn}_{0.1}\text{Cu}_{0.1}\text{O}_2$ is sensitive to the cycling history. Moreover, it may suggest that greater structural stability upon cycling for $\text{P2-Na}_{2/3}\text{Mn}_{0.8}\text{Zn}_{0.1}\text{Cu}_{0.1}\text{O}_2$ can be achieved by applying a higher current on the first cycle. In a similar manner to the improved performance of the hard carbon and carbon nanotube composite electrode at higher current rates reported by Rangom et al.,^[27] the enhanced structural stability of $\text{P2-Na}_{2/3}\text{Mn}_{0.8}\text{Zn}_{0.1}\text{Cu}_{0.1}\text{O}_2$ could be associated with the formation of a more optimal electrolyte-interface layer upon applying a higher initial current rate.

2.2. P2- $\text{Na}_{2/3}\text{Mn}_{0.8}\text{Zn}_{0.1}\text{Ti}_{0.1}\text{O}_2$

Given the appearance of an additional reflection at $2\theta = 14.42^\circ$ (2.6 \AA) for the $\text{P2-Na}_{2/3}\text{Mn}_{0.8}\text{Zn}_{0.1}\text{Cu}_{0.1}\text{O}_2$ composition, an additional lower rate (25 mA.g^{-1}) experiment was performed for $\text{P2-Na}_{2/3}\text{Mn}_{0.8}\text{Zn}_{0.1}\text{Ti}_{0.1}\text{O}_2$, see Table S4 for cycling conditions. Figure 9 shows the refinement for the initial dataset prior to cycling; the uncycled material adopts $P6_3/mmc$ symmetry with refined lattice parameters of $a = 2.9034(2) \text{ \AA}$ and $c = 11.2220(2) \text{ \AA}$ – crystallographic details can be found in Table S5.

The phase evolution is primarily solid solution and was modelled with P2 phases (space group $P6_3/mmc$). Evolution of the 002, 100 and 101 reflections are shown in Figure 10 and the resulting evolution in lattice parameters and unit cell volume as a function of time is shown in Figure 11, together with the potential profile. Upon charging, the initial P2-type phase evolves to form two P2-type phases around 3.12 V or 54 minutes. The difference in c lattice parameters between the two phases is likely due to differences in Na-content (i.e., Na-rich/Na-poor phases with respectively smaller/larger c lattice

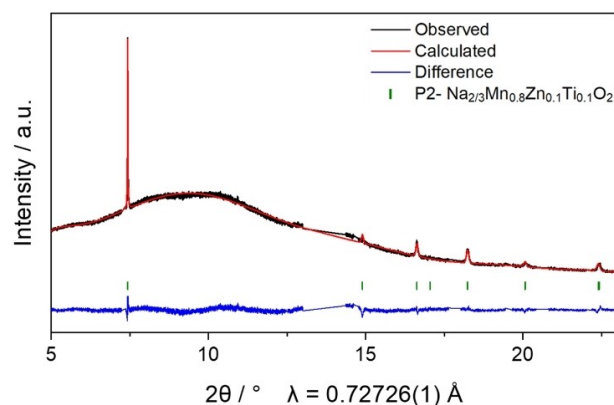


Figure 9. Rietveld refined fit of the uncycled $\text{P2-Na}_{2/3}\text{Mn}_{0.8}\text{Zn}_{0.1}\text{Ti}_{0.1}\text{O}_2$ electrode, within a modified Na half-cell.

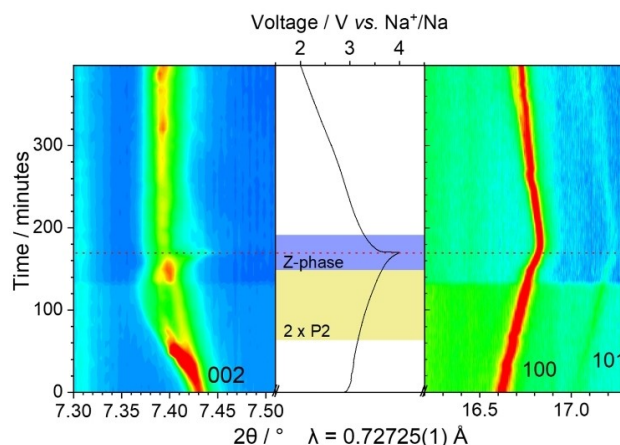


Figure 10. Selected 2θ regions of operando synchrotron XRD data and potential profile as a function of time highlighting the evolution of the 002, 100 and 101 reflections for $\text{P2-Na}_{2/3}\text{Mn}_{0.8}\text{Zn}_{0.1}\text{Ti}_{0.1}\text{O}_2$ cycled at the lower current rate of 25 mA.g^{-1} . Single phase, two phase and Z phase regions are shown in white, yellow and purple respectively.

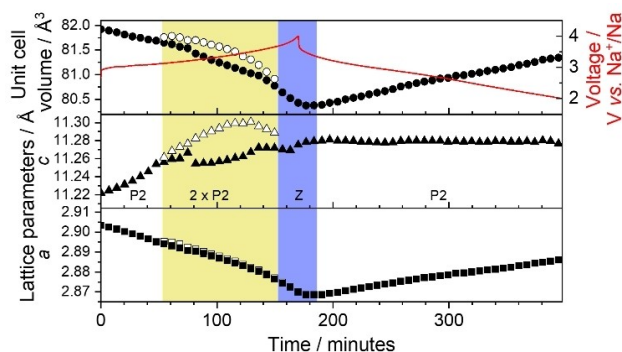


Figure 11. Electrochemical profile, change in unit cell volume, c and a lattice parameters as a function of time for P2- $\text{Na}_{2/3}\text{Mn}_{0.8}\text{Zn}_{0.1}\text{Ti}_{0.1}\text{O}_2$. Single phase, two phase and Z phase regions are shown in white, yellow and purple respectively.

parameters). Preceding the transformation from the ordered P2-type phases to the less ordered Z phase around 3.68 V or 153 minutes, a noticeable contraction in the c lattice parameter for the P2- type phase with the larger c lattice parameter (and therefore lower Na-content) is observed, which is indicative of transition metal migration into the sodium layer.^[13] Evidence of an intergrowth, or Z phase, structure close to the charged state is shown in Figure S3 in the Supporting Information. In comparison to the charged state of P2- $\text{Na}_{2/3}\text{Mn}_{0.8}\text{Zn}_{0.1}\text{Cu}_{0.1}\text{O}_2$ charged to 4.0 V at the same current rate of $25 \text{ mA}\cdot\text{g}^{-1}$, a greater degree of intergrowth seems to take place, as indicated by the additional small peak at a smaller d spacing shown in Figure S4 in the Supporting Information.

Upon discharge, the c lattice parameter remains stable. The occurrence of a stable c lattice parameter upon discharge has been previously observed for the related Zn-containing compositions P2- $\text{Na}_{2/3}\text{Mn}_{0.8}\text{Zn}_{0.1}\text{Cu}_{0.1}\text{O}_2$ and P2- $\text{Na}_{2/3}\text{Mn}_{0.8}\text{Zn}_{0.1}\text{Al}_{0.1}\text{O}_2$ at a higher current rate of $40 \text{ mA}\cdot\text{g}^{-1}$. If the migration of transition metals into the sodium layer, indicated by the c lattice parameter contraction near the end of 1st charge as discussed above, is irreversible on the beginning of discharge, it would seem reasonable to suggest that the residual transition metal ions in the sodium layers could be trapped in the transition metal layer, hence possibly stabilizing the layered structure. However, if as reported for NaFeO_2 , too much irreversible transition metal migration takes place, Na-ion diffusion may become hindered, thus limiting the available capacity.^[14] Note the P2- $\text{Na}_{2/3}\text{Mn}_{0.8}\text{Zn}_{0.1}\text{Cu}_{0.1}\text{O}_2$ at $25 \text{ mA}\cdot\text{g}^{-1}$ appears to show reversibility of the c lattice contraction near the end of 1st charge with an expansion during initial discharge (see Figure 3).

When P2- $\text{Na}_{2/3}\text{Mn}_{0.8}\text{Zn}_{0.1}\text{Ti}_{0.1}\text{O}_2$ is cycled at the faster current rate of $40 \text{ mA}\cdot\text{g}^{-1}$ for the first cycle, as previously reported,^[15] single phase solid-solution behavior is observed throughout and the collapse in c lattice parameter close the charged state is much less significant (see Figure S5 in the Supporting Information). The smaller structural changes observed at the higher current rate are likely associated with the lower capacity (57 vs. $67 \text{ mAh}\cdot\text{g}^{-1}$) and therefore smaller amount of sodium ions deintercalated from the structure. Moreover, during the subsequent discharge cycle, conventional contraction in the c

lattice parameter is observed at the faster current rate, which would be in keeping the hypothesis that residual migrated transition metal ions could be stabilizing the structure at the lower current rate of $25 \text{ mA}\cdot\text{g}^{-1}$.

2.3. Comparison of P2- $\text{Na}_{2/3}\text{Mn}_{0.8}\text{Zn}_{0.1}\text{Cu}_{0.1}\text{O}_2$ and P2- $\text{Na}_{2/3}\text{Mn}_{0.8}\text{Zn}_{0.1}\text{Ti}_{0.1}\text{O}_2$

The crystallographic details for the two materials, P2- $\text{Na}_{2/3}\text{Mn}_{0.8}\text{Zn}_{0.1}\text{Cu}_{0.1}\text{O}_2$ ($a = 2.9080(2) \text{ \AA}$, $c = 11.1867(1) \text{ \AA}$) and P2- $\text{Na}_{2/3}\text{Mn}_{0.8}\text{Zn}_{0.1}\text{Ti}_{0.1}\text{O}_2$ ($a = 2.9034(2) \text{ \AA}$, $c = 11.2220(2) \text{ \AA}$), can be found in Tables S2 and S5 in the Supporting Information, respectively. While a larger c lattice parameter might be expected for P2- $\text{Na}_{2/3}\text{Mn}_{0.8}\text{Zn}_{0.1}\text{Cu}_{0.1}\text{O}_2$ due to the larger crystal radius of Cu^{2+} (0.870 \AA) compared to Ti^{4+} (0.745 \AA), it should be noted that high spin Mn^{3+} (0.785 \AA) has a larger radius relative to Mn^{4+} (0.670 \AA) and therefore the lattice parameters may also be highly sensitive to changes in proportion of $\text{Mn}^{3+/4+}$, as well the materials Na content.^[23] Hence, in the follow discussion care has been taken to compare the overall trends in structural evolution as opposed to the specific details of the two datasets.

Comparable phase evolution on first charge (P2 \rightarrow $2 \times$ P2 \rightarrow Z) is observed for both P2- $\text{Na}_{2/3}\text{Mn}_{0.8}\text{Zn}_{0.1}\text{Cu}_{0.1}\text{O}_2$ and P2- $\text{Na}_{2/3}\text{Mn}_{0.8}\text{Zn}_{0.1}\text{Ti}_{0.1}\text{O}_2$ at the slower current rate of $25 \text{ mA}\cdot\text{g}^{-1}$. However, no additional reflection close to the charged state is observed for P2- $\text{Na}_{2/3}\text{Mn}_{0.8}\text{Zn}_{0.1}\text{Ti}_{0.1}\text{O}_2$, see Figure S6 in the Supporting Information. Understanding the basis of the reflection located at a d spacing of 2.6 \AA is work in progress. Furthermore, both P2- $\text{Na}_{2/3}\text{Mn}_{0.8}\text{Zn}_{0.1}\text{Cu}_{0.1}\text{O}_2$ and P2- $\text{Na}_{2/3}\text{Mn}_{0.8}\text{Zn}_{0.1}\text{Ti}_{0.1}\text{O}_2$ display fewer structural transitions when first cycled at a faster current rate of $40 \text{ mA}\cdot\text{g}^{-1}$ compared with $25 \text{ mA}\cdot\text{g}^{-1}$. This highlights the importance of optimizing the compromise between deliverable capacity and long term cyclability (minimizing the number of structural transitions) of sodium layered oxide cathode materials.

On discharge at $25 \text{ mA}\cdot\text{g}^{-1}$, the structural transformations that took place during the 1st charge cycle appear to be more reversible for the P2- $\text{Na}_{2/3}\text{Mn}_{0.8}\text{Zn}_{0.1}\text{Cu}_{0.1}\text{O}_2$ than P2- $\text{Na}_{2/3}\text{Mn}_{0.8}\text{Zn}_{0.1}\text{Ti}_{0.1}\text{O}_2$. However, the c lattice parameter during discharge seems to be more stable for P2- $\text{Na}_{2/3}\text{Mn}_{0.8}\text{Zn}_{0.1}\text{Ti}_{0.1}\text{O}_2$. Since good capacity retention have been reported for P2- $\text{Na}_{2/3}\text{Mn}_{0.8}\text{Zn}_{0.1}\text{Cu}_{0.1}\text{O}_2$ (87.5%) and P2- $\text{Na}_{2/3}\text{Mn}_{0.8}\text{Zn}_{0.1}\text{Ti}_{0.1}\text{O}_2$ (85.9%) upon cycling between 2.0–4.0 V at $C/10$ ($\sim 25 \text{ mA}\cdot\text{g}^{-1}$) for 50 cycles, this would imply that both the reversibility of structural transitions and stability of the c lattice parameter are important factors to consider when developing NIB cathode materials.

2.4. Comparison with Reported Variable Current Literature

Comparable electrochemical properties have been reported for both P2- $\text{Na}_{2/3}\text{Mn}_{0.9}\text{Fe}_{0.1}\text{O}_2$ and P2- $\text{Na}_{2/3}\text{Mn}_{0.8}\text{Zn}_{0.1}\text{Cu}_{0.1}\text{O}_2$; at a rate of $C/10$ ($\sim 25 \text{ mA}\cdot\text{g}^{-1}$) and voltage window of 4.0–2.0 V, the former displays a 2nd discharge capacity of $158.46 \text{ mAh}\cdot\text{g}^{-1}$ and a capacity retention of 91% after 18 cycles while these values

are 159.02 mAh.g⁻¹ and 92 % (after 25 cycles) for the latter. Considering the structural evolution, no ordering reflections or indications of transition metal migration were reported for P2-Na_{2/3}Mn_{0.9}Fe_{0.1}O₂ upon charging. However, throughout discharge, both materials display primarily solid-solution behaviour.

Conversely, the P2-Na_{2/3}Mn_{1/3}Fe_{2/3}O₂ cathode material displays a capacity retention of 81 % after only 10 cycles at C/10, between 4.2–1.5 V.^[24] For further context, the P2-Na_{2/3}Mn_{0.8}Zn_{0.1}Cu_{0.1}O₂ displays a capacity retention of 87 % after 50 cycles between 2.0–4.0 V, also at a rate of C/10.^[6] Although the electrochemical performance cannot be compared directly due to the different potential windows used, the greater reversibility of the structural transitions upon cycling P2-Na_{2/3}Mn_{0.8}Zn_{0.1}Cu_{0.1}O₂ would be in keeping with the better long term cyclability reported. When cycled at a slow current rate of C/16 (~15 mA.g⁻¹), the P2-Na_{2/3}Mn_{1/3}Fe_{2/3}O₂ material displayed a P2-OP4 phase transition, which was found to persist until the discharged state.^[10] Moreover, when cycled at the higher rate of 1 C (~240 mA.g⁻¹), a new two-phase region emerged during discharge. For P2-Na_{2/3}Mn_{0.8}Zn_{0.1}Cu_{0.1}O₂, formation of the disordered Z phase takes place close to the charged state but notably: the phase transformation was found to be highly reversible; the disordered phase was not found to persist until the discharge state; and no new phases were detected at low voltages at any of the rates tested.^[15] The more stable discharged state observed for P2-Na_{2/3}Mn_{0.8}Zn_{0.1}Cu_{0.1}O₂ is most likely due to Mn rich composition and the incorporation of the Zn²⁺ and Cu²⁺ dopants. The substitution of M for cations with a formal oxidation state of +2 (as compared to Fe³⁺), increases the proportion of Mn⁴⁺ relative to Mn³⁺ in the material, which helps to mitigate Jahn-Teller distortion associated with the presence of Jahn-Teller active Mn³⁺, primarily at the discharged state at which maximum sodiation takes place.

3. Conclusion

Through variable current rate operando XRD data collected for P2-Na_{2/3}Mn_{0.8}Zn_{0.1}Cu_{0.1}O₂, phase evolution is shown to be dependent on the current, choice of voltage cut-off, and cycling history used. As such, the relevance of evaluating structural changes and reaction mechanisms that take place during the initial cycle of device operation is demonstrated. The data also revealed the reversible formation of an ordering reflection at high voltages. Comparable phase evolution on first charge (P2→2×P2→Z) is observed for both P2-Na_{2/3}Mn_{0.8}Zn_{0.1}Cu_{0.1}O₂ and P2-Na_{2/3}Mn_{0.8}Zn_{0.1}Ti_{0.1}O₂ at a slower current rate of 25 mA.g⁻¹ and this differs to using a 1st charge current rate of 40 mA.g⁻¹ which highlights the significance of initial applied current rate on the structural evolution of layered materials. Notably, no additional ordering reflection was observed for P2-Na_{2/3}Mn_{0.8}Zn_{0.1}Ti_{0.1}O₂ close to the charged state. Moreover, at the lower current rate of 25 mA.g⁻¹ (compared with 40 mA.g⁻¹), a more pronounced collapse in the P2-Na_{2/3}Mn_{0.8}Zn_{0.1}Ti_{0.1}O₂ c lattice parameter (which can be indicative of transition metal migration) may be observed upon charge, followed by fewer

structural changes on the subsequent discharge. This may be due to the presence of residual transition metal ions in the sodium layer stabilising the structure. For Na_{2/3}Mn_{0.8}Zn_{0.1}Cu_{0.1}O₂ reversible phase evolution initiating at similar Na concentrations on cycling was evidenced at current rates of 25, 50 and 100 mA.g⁻¹ and when extending the voltage window from 4 to 4.5 V. The discharged state was a stable single-phase material while Z-type intergrowth was found at the charged state. This work demonstrates that when developing new cathode materials it is important to consider not only compositional influence on the electrochemistry but also the structural evolution as a function of applied current, potential cut-offs and cycling history on the electrochemistry as such information can provide information on the possible longevity of the electrode.

Experimental Section

P2-Na_{2/3}Mn_{0.8}Zn_{0.1}Cu_{0.1}O₂ and P2-Na_{2/3}Mn_{0.8}Zn_{0.1}Ti_{0.1}O₂ were prepared via a solid-state technique. Stoichiometric amounts of Na₂CO₃ (Sigma Aldrich, anhydrous), Mn₂O₃ (Alfa Aesar, purity: 98 %), ZnO (Sigma Aldrich, 99.0 %), CuO (Alfa Aesar, 99.7 %) and TiO₂ (Alfa Aesar, 99.9 %), were mixed using a planetary ball milling (Pulverisette7, Fritsch) and the resulting powders were pressed into 20 mm diameter pellets. The pellets were subsequently calcined under air at 1000 °C for 12 hours, then slowly cooled to 200 °C. The samples were then rapidly transferred to an Argon-filled glove box (M-BRAUN) for storage. Details regarding the chemical, electrochemical and initial structural characterisation of the materials can be found in refs. [6] and [15].

Electrode preparation was carried out in an Ar-filled glove box. The electrode slurry was prepared by mixing the active material, carbon black, and poly(vinylidene difluoride) (PVDF) in a mass ratio of 80:10:10 in N-methyl-2-pyrrolidone (NMP) followed by vigorous magnetic stirring for 2 hours. Subsequently, the slurry was cast onto an aluminium current collector foil using a mini coater (Hoshen) and dried in a vacuum oven at 120 °C for 12 hours. Electrodes were punched out and pressed at 3538.6 kg/cm² before being assembled in the battery.

Na half cells with 3 mm diameter Kapton-covered windows in the casing and 5 mm diameter holes in the stainless spacer were used for the construction of the coin cells for the operando XRD measurements. The CR2032 coin cells were constructed in an Ar-filled glove box and contained Na metal as the anode (~1 mm thickness), a glass fibre separator and 1 M NaPF₆ in ethylene carbonate (EC) : dimethyl carbonate (DMC) (EC/DMC, 1:1 v/v) electrolyte solution. To enable comparison to previous studies, no additives such as fluoroethylene carbonate (FEC) were used. Synchrotron XRD experiments were performed 1–2 days after cell construction. Further details regarding coin cell construction and beamline setup can be found in our previous publications.^[25]

Operando synchrotron XRD data were collected on the Powder Diffraction beamline at the Australian Synchrotron for which the wavelength was determined by refining a structural model with data collected on a NIST 660b LaB₆ standard reference material. XRD data were collected every 3.4 minutes (with detector position movement) on the coin cell in transmission geometry. Details regarding the wavelength and charge/discharge cycles of each sample can be found in Tables S1 and S2 in the Supporting Information. Rietveld refinements were carried out using the software package GSAS.^[26] The EXPGUI software interface was used with GSAS.^[27] For analysis of the data, reflections which are not

present in the as synthesised powder sample and do not change position/intensity upon cycling were excluded as well as reflections corresponding to the aluminium current collector and sodium metal.

Acknowledgements

Jenny Stansby acknowledges UNSW/ANSTO for the PhD scholarship. The authors would also like to acknowledge the financial support of the Australian Research Council Discovery programs DP200100959/FT200100707 and of the Spanish Ministerio de Economía y Competitividad through the project ENE2016-75242-R. Part of this research was undertaken on the PD beamline at the Australian Synchrotron, part of ANSTO.

Conflict of Interest

The authors declare no conflict of interest.

Keywords: cathode materials · manganese · operando studies · sodium layered oxides · structural evolution

- [1] J.-Y. Hwang, S.-T. Myung, Y.-K. Sun, *Chem. Soc. Rev.* **2017**, *46*, 3529–3614.
- [2] R.-M. Gao, Z.-J. Zheng, P.-F. Wang, C.-Y. Wang, H. Ye, F.-F. Cao, *Energy Storage Mater.* **2020**, *30*, 9–26.
- [3] N. Ortiz-Vitoriano, N. E. Drewett, E. Gonzalo, T. Rojo, *Energy Environ. Sci.* **2017**, *10*, 1051–1074.
- [4] C. Delmas, C. Fouassier, P. Hagenmuller, *Physica B + C* **1980**, *99*, 81–85.
- [5] a) A. Caballero, L. Hernán, J. Morales, L. Sánchez, J. Santos Peña, M. A. G. Aranda, *J. Mater. Chem.* **2002**, *12*, 1142–1147; b) S. Kumakura, Y. Tahara, K. Kubota, K. Chihara, S. Komaba, *Angew. Chem. Int. Ed. Engl.* **2016**, *55*, 12760–12763.
- [6] E. Gonzalo, N. Ortiz-Vitoriano, N. E. Drewett, B. Acebedo, J. M. López del Amo, F. J. Bonilla, T. Rojo, *J. Power Sources* **2018**, *401*, 117–125.
- [7] a) R. J. Clément, J. Billaud, A. Robert Armstrong, G. Singh, T. Rojo, P. G. Bruce, C. P. Grey, *Energy Environ. Sci.* **2016**, *9*, 3240–3251; b) M. H. Han, E. Gonzalo, N. Sharma, J. M. López Del Amo, M. Armand, M. Avdeev, J. J. Saiz Garitaonandia, T. Rojo, *Chem. Mater.* **2016**, *28*, 106–116.
- [8] D. Goonetilleke, J. H. Stansby, N. Sharma, *Curr. Opin. Electrochem.* **2019**, *15*, 18–26.
- [9] N. Sharma, N. Tapia-Ruiz, G. Singh, A. R. Armstrong, J. C. Pramudita, H. E. A. Brand, J. Billaud, P. G. Bruce, T. Rojo, *Chem. Mater.* **2015**, *27*, 6976–6986.
- [10] N. Sharma, M. H. Han, J. C. Pramudita, E. Gonzalo, H. E. A. Brand, T. Rojo, V. K. Peterson, T. Rojo, X. Huang, Z. Ogumi, A. Wattiaux, C. Delmas, *J. Mater. Chem. A* **2015**, *3*, 21023–21038.
- [11] W. M. Dose, N. Sharma, J. C. Pramudita, M. Avdeev, E. Gonzalo, T. Rojo, *Chem. Mater.* **2018**, *30*, 7503–7510.
- [12] a) J. M. Paulsen, J. R. Dahn, *Solid State Ionics* **1999**, *126*, 3–24; b) N. Bucher, S. Hartung, J. B. Franklin, A. M. Wise, L. Y. Lim, H.-Y. Chen, J. N. Weker, M. F. Toney, M. Srinivasan, *Chem. Mater.* **2016**, *28*, 2041–2051; c) W. Kang, Z. Zhang, P.-K. Lee, T.-W. Ng, W. Li, Y. Tang, W. Zhang, C.-S. Lee, D. Y. Wai Yu, *J. Mater. Chem. A* **2015**, *3*, 22846–22852; d) M. Bianchini, E. Gonzalo, N. E. Drewett, N. Ortiz-Vitoriano, J. M. López del Amo, F. J. Bonilla, B. Acebedo, T. Rojo, *J. Mater. Chem. A* **2018**, *6*, 3552–3559; e) G. Singh, N. Tapia-Ruiz, J. M. Lopez del Amo, U. Maitra, J. W. Somerville, A. R. Armstrong, J. Martinez de Ilarduya, T. Rojo, P. G. Bruce, *Chem. Mater.* **2016**, *28*, 5087–5094.
- [13] D. Goonetilleke, S. Wang, E. Gonzalo, M. Galcerán, D. Saurel, S. J. Day, F. Fauth, T. Rojo, N. Sharma, *J. Mater. Chem. A* **2019**, *7*, 12115–12125.
- [14] B. Silvan, E. Gonzalo, L. Djuandhi, N. Sharma, F. Fauth, D. Saurel, *J. Mater. Chem. A* **2018**, *6*, 15132–15146.
- [15] J. Stansby, N. Sharma, M. Avdeev, H. E. A. Brand, B. Johannessen, E. Gonzalo, N. E. Drewett, N. Ortiz-Vitoriano, T. Rojo, *Chem. Mater.* **2020**.
- [16] X. Li, X. Ma, D. Su, L. Liu, R. Chisnell, S. P. Ong, H. Chen, A. Toumar, J. C. Idrobo, Y. Lei, J. Bai, F. Wang, J. W. Lynn, Y. S. Lee, G. Ceder, *Nat. Mater.* **2014**, *13*, 586–592.
- [17] K. Wang, P. Yan, Z. Wang, J. Fu, Z. Zhang, X. Ke, M. Sui, *J. Mater. Chem. A* **2020**, *8*, 16690–16697.
- [18] J. W. Somerville, A. Sobkowiak, N. Tapia-Ruiz, J. Billaud, J. G. Lozano, R. A. House, L. C. Gallington, T. Ericsson, L. Häggström, M. R. Roberts, U. Maitra, P. G. Bruce, *Energy Environ. Sci.* **2019**, *12*, 2223–2232.
- [19] C. Ma, J. Alvarado, J. Xu, R. J. Clément, M. Kodur, W. Tong, C. P. Grey, Y. S. Meng, *J. Am. Chem. Soc.* **2017**, *139*, 4835–4845.
- [20] a) X. Bai, M. Sathiy, B. Mendoza-Sánchez, A. Iadecola, J. Vergnet, R. Dedryvère, M. Saubanère, A. M. Abakumov, P. Rozier, J.-M. Tarascon, *Adv. Energy Mater.* **2018**, *8*; b) R. A. House, U. Maitra, L. Jin, J. G. Lozano, J. W. Somerville, N. H. Rees, A. J. Naylor, L. C. Duda, F. Massel, A. V. Chadwick, S. Ramos, D. M. Pickup, D. E. McNally, X. Lu, T. Schmitt, M. R. Roberts, P. G. Bruce, *Chem. Mater.* **2019**, *31*, 3293–3300.
- [21] X. Rong, E. Hu, Y. Lu, F. Meng, C. Zhao, X. Wang, Q. Zhang, X. Yu, L. Gu, Y.-S. Hu, H. Li, X. Huang, X.-Q. Yang, C. Delmas, L. Chen, *Joule* **2019**, *3*, 503–517.
- [22] a) D. H. Lee, J. Xu, Y. S. Meng, *Phys. Chem. Chem. Phys.* **2013**, *15*, 3304–3312; b) A. Gutierrez, W. M. Dose, O. Borkiewicz, F. Guo, M. Avdeev, S. Kim, T. T. Fister, Y. Ren, J. Bareño, C. S. Johnson, *J. Phys. Chem. C* **2018**, *122*, 23251–23260.
- [23] R. D. Shannon, *Acta Crystallogr. A* **1976**, *32*, 751–767.
- [24] N. Sharma, E. Gonzalo, J. C. Pramudita, M. H. Han, H. E. A. Brand, J. N. Hart, W. K. Pang, Z. Guo, T. f. Rojo, *Adv. Funct. Mater.* **2015**, *25*, 4994–5005.
- [25] R. J. Gummow, N. Sharma, R. Feng, G. Han, Y. He, *J. Electrochem. Soc.* **2013**, *160*, A1856.
- [26] A. C. Larson, R. B. Von Dreele in *General structure analysis system (GSAS)*, Los Alamos National Laboratory: Los Alamos, NM, USA, **2004**.
- [27] B. Toby, *J. Appl. Crystallogr.* **2001**, *34*, 210–213.

Manuscript received: December 26, 2020